Materials Research. 2022; 25:e20220118
DOI: https://doi.org/10.1590/1980-5373-MR-2022-0118

Effect of the Heat Input and Ageing Treatment on Microstructure and Mechanical Properties of AISI 317L Stainless Steel Dissimilar Welded Joints

Pedro Duarte Antunes*[a], *Cleiton Carvalho Silva*[b], *Edmilson Otoni Corrêa*[c]

[a]*Centro Federal de Educação Tecnológica de Minas Gerais, (CEFET/MG), Departamento de Formação Geral, Varginha, MG, Brasil.*
[b]*Universidade Federal do Ceará (UFC), Laboratório de Pesquisa e Tecnologia de Soldagem (LPTS), Fortaleza, CE, Brasil.*
[c]*Universidade Federal de Itajubá (UNIFEI), Departamento de Engenharia Mecânica, Itajubá, MG, Brasil.*

Received: March 12, 2022; Revised: July 11, 2022; Accepted: August 10, 2022

The present work investigated the influence of heat input and aging time on the microstructural characteristics and the mechanical properties of dissimilar AISI 317L austenitic stainless steel welded joints. The AWS ER2209 wire-electrode was used as filler metal, and two different heat input levels were applied (4 and 8 kJ/cm), aiming to verify the influence of this parameter on the deleterious phases precipitation. An aging heat treatment (AHT) was carried out at 700 °C for two different exposure times: 50 and 100 hours. It was observed that aging promoted a refinement of the base metal region, and all delta ferrite was transformed into the sigma phase. The microstructure of the fusion zone (without AHT) presented a significant amount of austenite that precipitated in three different morphologies: allotriomorphific of grain boundary, Widmanstätten, and intragranular. For all the thermally treated samples, it was possible to identify the presence of the σ and χ phases. Additionally, the highest concentration of the χ phase was identified in the samples submitted to 50 hours of AHT. The welding condition and AHT that presented joints with higher mechanical resistance and remarkable toughness were those welded with 4 kJ/cm heat input and with 100 hours of AHT. All welded joints showed an increase in the hardness profile after AHT. The microhardness values showed a good correlation with the microstructure and the mechanical tests so that the highest values of microhardness were observed in welded joints with heat input of 4 kJ/cm and 100 hours of AHT

Keywords: *AISI 317L Steel, Electrode AWS ER2209, Aging heat treatment, Microstructure, mechanical properties.*

1. Introduction

Petroleum is a fluid containing, besides hydrocarbon, many contaminants in low or high levels in its composition. Among the primary contaminants, it can be highlighted the hydrogen sulfide (H_2S), naphthenic acids ($R(CH_2)nCOOH$), water (H_2O), carbon dioxide (CO_2), sand, and others[1,2]. Carbon dioxide can also combine with water molecules resulting in carbonic acid (H_2CO_4)[3]. Along to the production and processing chain of oil and gas, there are several steps in which the medium may become extremely acidic. Due to the high levels of contaminants existing in Brazilian oils, notably concerning to naphthenic acids, carbonic acid, hydrogen sulfide, in addition to their high concentration of chlorides (Cl^-), its corrosivity has been considered one of the main operational problem in oil refining settings[4-6], becoming necessary the use of materials resistant to corrosion. In the design of these processing plants, stainless steels with a higher amount of Mo, such as the AISI 317L, have a prominent place due to its remarkable chemical composition, which enables the steel to protect itself when in contact with an oxidizing species. This protection is related to a compact, adhered, impermeable, and Cr_2O_3 thin layer, which passivates the steel against the action of the acids[7]. The use of advanced steel can significantly contribute to reducing the maintenance costs associated with repairing the processing equipment, besides increasing productivity.

The welding of advanced engineering materials for equipment and components manufacturing is a relevant task, requiring the proper setup, welding parameters and filler metal choice. Usually, many materials can be successfully welded by matching materials with similar microstructure and chemical composition features. However, for some specific applications, dissimilar metal welding has been required to join different materials or to confer the joint an improved characteristic for the fusion zone by introducing alloying elements or a desirable microstructure.

During the dissimilar welding of components involving Mo-rich austenitic stainless steel is necessary to develop a process procedure that offers the expected productivity and guarantees an as stable as possible microstructure with assured metallurgical changes in the fusion zone (FZ) and heat-affected zone (HAZ) to enhance the properties of the welded joint. However, this stability can not be achieved when

*e-mail: ecotoni@unifei.edu.br

Mo-rich austenitic stainless steel HAZ and FZ are exposed to critical temperatures (above 800 ºC) during manufacturing steps like welding, hot bend, wrought, heat treatments, or even due to unusual overheating during processing. (above 800 ºC), Exposures in this temperature range induce the formation of secondary phases such as σ and χ may occur and modify the local corrosion and mechanical properties of these materials[4-7].

Additionally, the solidification process can introduce some metallurgical effects that impair the fusion zone's properties requiring the use of overmatched filler metals. Traditionally, for austenitic stainless steel welds operating in harsh environments in which the fusion zone represents a critical point, the replacement of the similar filler metal for another one with a boosted chemical composition has been recommended, as 309MoL filler metal. However, this option is not feasible when the base metal has higher Mo content, as in the case of 317L steel. Among the options available in the market for dissimilar welding is the duplex stainless steel, containing at least the same content of Mo, with an increased concentration of Cr.

Several works[8-10], which studied dissimilar welding among austenitic stainless steels and other types of stainless steels, have reported that higher delta-ferrite formation in the weld metal associated with higher Mo concentration contributes to the precipitation of these deleterious secondary phases, leading to a decrease of the pitting and stress corrosion cracking resistance of the welded joint. Additionally, as the δ-ferrite is more easily electrochemical attacked than austenite, the corrosion process may be accelerated depending on the environment.

In other words, oil and gas industry welding engineers have a great interest in knowing better the phase transformation and precipitation that occur during dissimilar welding of austenitic stainless steels to make a better choice of the welding parameters and mitigate metallurgical failures (stress corrosion cracking, pitting corrosion, etc.) in similar or dissimilar welded joints of these materials.

In this sense, an important issue has been the evaluation of proper filler metals for welds of Mo-rich stainless steels, such as the AISI 317L stainless steel, specified for critical applications in onshore and offshore oil and gas processing units, chemical and petrochemical plants, paper and pulp industries and other facilities.For that, an investigation of the filler metal chemical composition relation to the δ-ferrite amount and to the elemental partitioning in the weld metal and HAZ has been carried out to keep the corrosion and mechanical properties of the welded joint similar to the base metal. Recently, duplex stainless steels have been investigated as filler metal to weld Mo-rich austenitic stainless steels to mitigate metallurgical and mechanical problems that arise due to the secondary phases precipitations during welding of austenitic stainless steels[8-13]. However, no studies were found in the literature specifically regarding this application for the 317L steel.

In sum, the study of the effect of the welding parameters and AHT on dissimilar welded joints of Mo-rich austenitic stainless steels using duplex stainless steel filler metal and the robotic-pulsed GMAW process is scarce and of undoubted importance for the oil and gas industries. Specifically, for offshore installations, given the great aggressiveness of the marine environment and the exposure of equipment to oils with high acidity.

Therefore, the objective of the present work was to study the influence of the heat input and pos-welding aging heating treatment (AHT) on the microstructure and mechanical properties of welded joints of AISI 317L stainless steel using the duplex stainless steel AWS ER2209 electrode. The most important contribution of this study is the metallurgical change through quantitative microscopy and microanalysis evaluation under different processing conditions and how these secondary phases precipitation affects the hardness, strength and ductility of the dissimilar welded joint.

2. Experimental Procedure

For this study, AISI 317L stainless steel sheets of 3 mm thickness were used as base material and 1.2 mm diameter wire of duplex stainless steel ER2209 was used as filler metal. Table 1 presents the nominal chemical composition of the base and filler metal used obtained by optical emission spectroscopy (OES).

It can be noted from the Table 1 that the most significant difference in composition of the metals is the presence of N (austenite former) and a higher amount of Cr (ferrite former) in the ER2209 filler metal and a higher amount of Ni (austenite former) in the base metal.

The robotic welding was carried out with a single deposition on flat position on the 317L sheets using the pulsed-current GMAW process and two levels of heat input (4 and 8 Kj/cm). Table 2 shows the welding parameters adopted in this work.

After welding, the AHT of the samples were carried out in a muffle furnace at a temperature of 700 °C for 50 and 100 hours. Samples were taken from the welded joints cross-section before and after AHT. Such samples were prepared by grinding and polishing. After polishing, the samples were electrolytically etched with oxalic acid (10%) and nitric acid (20%) in addition to the attack by immersion in aqua regia for observation using optical microscopy.

Another set of polished samples had their microstructure analysed by Scanning Electron Microscopy in the backscattered electron (BSE) mode; which is very useful for identifying

Table 1. Chemical composition of AISI 317L austenitic stainless steel and AWS ER2209 electrode.

Composition (% weight)	Materials	
	AISI 317L	AWS ER2209
C	0.011	0.013
Cr	19.0	23.13
Ni	13.1	8.73
Mo	3.1	3.1
Mn	1.6	1.48
Si	0.4	0.51
P	0.02	0.02
S	0.003	0.0005
Co	-	0.039
Cu	-	0.12
N	-	0.15

Table 2. Welding parameters adopted.

Welding Parameters		
Heat Input (kJ/cm)	4	8
Peak Current (A)	250	240
Base Current (A)	65	100
Peak Time (s)	3	4.5
Base Time (s)	10	8
Frequency (Hz)	28 to 49	45 to 118
Average Current (A)	121	154
Effective Current (A)	139	165
Voltage (V)	19	26
Welding Speed (cm/min)	45	35
Wire Feed Speed. (m/min)	4.5	4.5
Gas Protection (flow)	Ar (99.99%)	Ar (99.99%)
	25 l/min	25 l/min

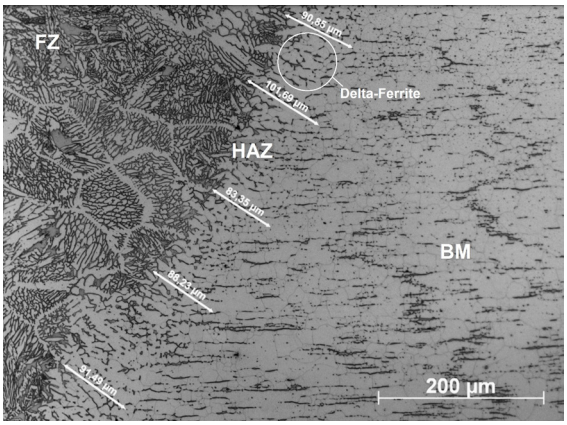

Figure 1. Microstructure of the HAZ of the welded joint with the AWS ER 2209 filler metal and heat input of 4KJ/cm.

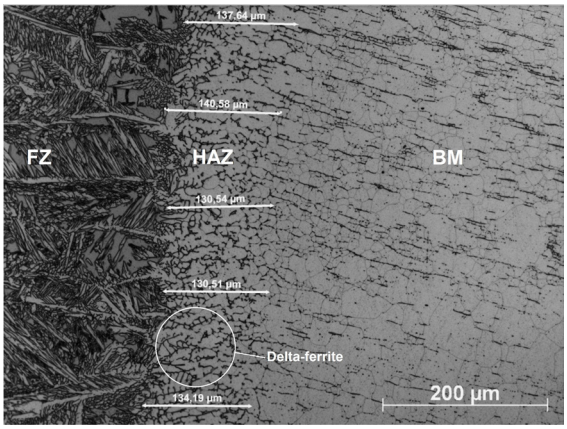

Figure 2. Microstructure of the HAZ of the welded joint with the AWS ER 2209 filler metal and heat input of 8 KJ/cm.

secondary phases. Based on these SEM images, a quantitative evaluation by image analysis was performed, using software developed by Albuquerque et al.[14], which allows to segment and quantify these images easily through neural networks.

In order to obtain a quantitative analysis of the ferrite content, a quantification of the phases present in the fusion zone and their average chemical composition were performed. For that, 50 images of each welding condition were recorded, and later, they were submitted to analysis using the SVRNA System software[15]. For comparative analysis, 50 measurements of the ferrite amount present in the FZ were also carried out for each welding condition using a ferritoscope.

Uniaxial tensile tests were performed to evaluate the tensile properties. The tensile sample geometries were in accordance with the ASTM G58 and ASTM E8 standard. Vickers microhardness in the transversal planes of the welded joints were measured with a load of 500 gf (HV 0.50) for 15 s using a digital microhardness tester.

3. Results and Discussion

3.1. Welded joints before AHT

Figures 1 and 2 show the microstructures of the HAZ of the dissimilar welded joints with heat inputs of 4 and 8 kJ/cm, respectively. In both the figures, the presence of measurements carried out in the area of the high temperature HAZ to estimate the average size of this region can be noted. This particular region (HT-HAZ) is characterized by a delta ferrite (dark phase) nucleation and its growth alongside the austenitic grains (grey phase) boundaries when the steel experiences temperatures above 1080 ºC. However, due to the sudden interruption of the phase transformation due to the fast heating, being not possible to ferritizing all structures even when heated within the entire ferrite field. Besides this incomplete austenite-to-ferrite phase transformation, there is not enough undercooling time to dissolve the delta ferrite produced during a heating cycle, frozen and remaining in the microstructure at room temperature. Quantitatively, it was possible to verify a more significant extension of the HT-HAZ (134.3 ± 13.72 µm) and rougher microstructure (presence of a semi-continuous network morphology) in the welded joints with 8 kJ/cm heat input. Corroborating with these findings, several studies have shown that in this type of dissimilar welding it is common to observe a microstructre partially fused with delta-ferrite dendrites in the austenitic grains boundaries in the fusion line (HAZ/FZ)[7,10,13,16,17].

Aguilar et al.[18] studying metallurgical transformations during dissimilar welding of the AISI 316L steel with AISI 430 ferritic steel, using two stainless steel electrodes (AWS E309L and AWS E2209-16), indicated that the size of the HT-HAZ and the average size of the coarse-grained ferrite depends directly on the welding heat input. On the other hand, the morphology and amount of ferrite are a function of the chemical composition of the filler metal, which changes the solidification mode. Nunes et al.[16] studied the influence of heat input on the HAZ of UNS S31803 duplex stainless steel welded joints using AWS E2209-17 coated electrode and two heat input levels (15 and 20 kJ/cm). They found that the variation in the heat input directly influenced the microstructure of the HAZ, so that the condition of higher heat input (20 kJ/cm) generated a coarsened grain and a more extensive unbalanced microstructure.

Figures 3 and 4 show microstructures of the fusion zone (FZ) of the dissimilar welded joints using 4 and 8 kJ / cm, respectively. A previous study performed by Antunes et al.[19],

using the AWS 317L as filler metal, found the presence of δ-ferrite within an austenitic matrix ranging from 8% to 12%, depending on the heat input. The morphology displayed by the δ-ferrite was vermicular (skeletal) and lathy (laminar), characteristics of filler metals solidifying into the ferritic-austenitic (FA) mode[10,20-22].

When the filler metal was changed to the AWS ER2209 duplex stainless steel, it was possible to notice a considerable increase in the ferrite fraction of the welded joints since the Cr and Mo contents of the duplex are higher than those of the AWS 317L; even though a significant amount of austenite has been observed in the weld metal due to the effect of temperature and the addition of nickel and nitrogen from the filler metal.

Based on the chemical composition of the AWS ER2209 electrode presented in Table 1, and using the Chromium (Equation 1) and Nickel (Equation 2) equivalent expressions proposed by Schaeffler[23] it were found the following values: 27.02 for Creq and 9.86 for the Nieq, which results in a Creq/Nieq ratio of 2.74. This information is essential to estimate the location of the filler metal on the pseudo-binary diagram shown in Figure 5[24]. Based on the Creq/Nieq ratio, it was found that the filler metal solidifies in the complete ferrite mode (F). In this case, ferrite is no longer the minority phase but the matrix, being the austenite formed in the ferrite grain boundaries after solidification due to a solid-state phase transformation at lower temperatures. When the same assessment was performed for the AWS 317L filler metal, the following values for the Creq and Nieq: 22.30 and 14.23, respectively, gave us a Creq/Nieq ratio of 1.57. According to the pseudo-binary diagram in Figure 4, this Creq/Nieq ratio falls into the FA solidification mode.

$$Creq = Cr + Mo + 1.5\,Si + 0.5\,Nb \quad \text{Equation 1}$$

$$Nieq = Ni + 30\,C + 0.5\,Mn \quad \text{Equation 2}$$

It is also noticed from the figures that there were no significant changes in the fusion zone microstructures of the welded joints for both heat input levels used. The formation of the ferrite phase with columnar morphology due to the solidification pattern and three primary austenite morphologies were observed in both conditions, which are grain boundary allotriomorphic, Widmanstätten and intragranular. These morphologies are typically found in duplex and super duplex stainless steels, agreeing with the literature[25,26], and differ significantly from those observed for the austenitic stainless steel metal welds, including 317L[9,19,27], because ferrite becomes more stable over a wide temperature range and the solid-state phase transformation from ferrite to austenite stars at a lower temperature.

From the WCR-1992 diagram and equations shown in Figure 6[28], it was possible to estimate the ferrite content in the fusion zone based on the chemical composition of the 2209 filler metal. It was calculated the Creq of 26.25 and the Nieq of 12.19, which results in a ferrite content ranging from 55% to 60%. Compared to the microstructure obtained for the AWS ER2209, the welds undoubtedly have a smaller

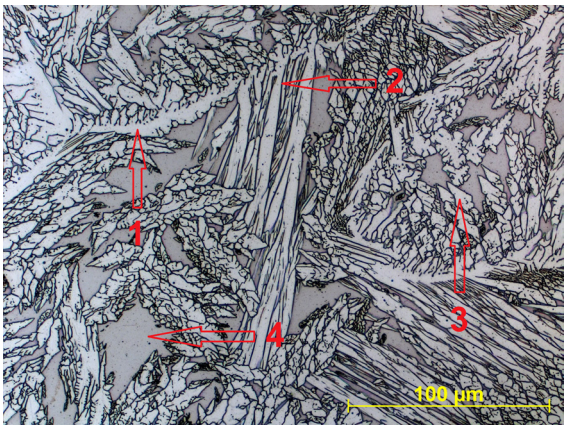

Figure 3. Microstructure of the FZ with the AWS ER2209 electrode using 4 KJ / cm. Highlight for points (1) γ Allotriomorphic grain contour, (2) γ Widmansttaten, (3) γ Intragranular and (4) Ferrite.

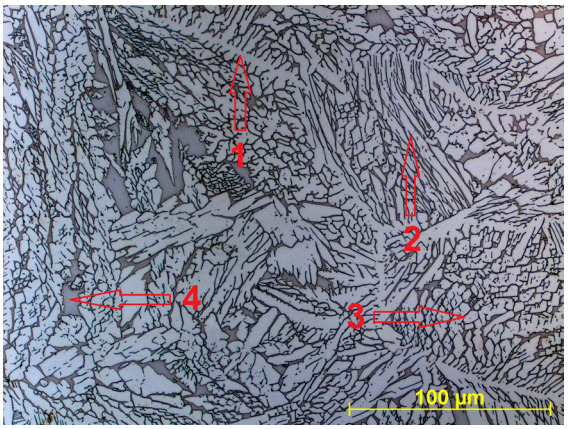

Figure 4. Microstructure of the FZ with the AWS ER2209 electrode using of 8 KJ / cm. Highlight for points (1) γ Allotriomorphic grain boundary, (2) γ Widmanstätten, (3) γ Intragranular and (4) Ferrite.

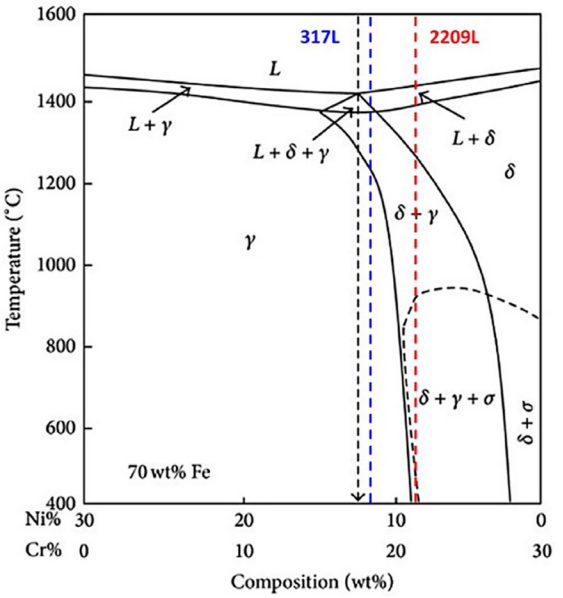

Figure 5. Fe-Cr-Ni pseudo-binary diagram[24].

amount of ferrite, but if compared to an austenite stainless steel filler metal, the ferrite content will be higher. However, further analysis is needed to quantify the fraction of each phase in both heat inputs.

Grain boundary allotriomorphic austenite, which is formed at high temperatures, nucleates heterogeneously in the grain boundaries of the ferrite during cooling, possibly being developed by a diffusional phase transformation mechanism. After the allotriomorphic austenite is formed along the grain boundary, the Widmanstätten morphology nucleates from the grain boundaries of the pre-existing ferrite or allotriomorphic austenite and grows along specific crystallographic planes of the matrix as parallel plates[18].

According to Muthupandia et al.[29], during heating, the transformation from austenite to ferrite generally occurs by diffusion of the interstitial and substitutional alloy elements such as C, Cr, Ni, N, etc. at temperatures above 1300°C. Among these alloying elements, nickel and nitrogen are critical because their diffusion controls the phase transformation in heating. However, these phase transformations are not governed by chemical composition. They are also affected by the thermal cycle since the cooling rate is directly related to the time to diffuse and the portioning the alloying elements between the ferrite and austenite phases[18].

Although significant differences in the fusion zones microstructures between 4 and 8 KJ/cm have not been found, is the knowledge that heat input also plays an essential role. Some studies have shown that, additionally to the nitrogen concentration, the use of higher heat inputs helps the welding of duplex stainless steels to achieve a well-balanced microstructure. It has also provided a more significant formation of Widmanstatten austenite, since adding nitrogen and extending the holding time at high temperatures facilitates the formation of Widmanstätten morphology[30,31].

The intragranular austenite, in turn, nucleus and precipitates in the ferrite grains generally at lower temperatures due to the supersaturation of the ferritic matrix with austenitizing elements[32]. It is worthwhile mentioning that this complex and particular morphology, composed of a ferritic matrix and precipitation of austenite in the three different forms (allotriomorphic grain boundary, Widmanstätten and intragranular) is closely related to the solidification mode (Mode F), in which ferrite is the only solidification phase with the later solid-state transformation from part of the ferrite to austenite. Table 3 presents the results obtained in quantifying ferrite in the fusion zone of the dissimilar welded joint.

Considering the percentage values of ferrite and their respective deviations shown in Table 3, it is clear that the variation of the heat input did not provoke significant changes in the amount of ferrite in the fusion zone, probably, as result of the high Cr content present in the AWS 2209 filler metal. The chemical compositions of both ferrite and austenite were obtained by EDS analyzes Average values of each alloying element found in the austenite and ferrite phases are shown in Table 4.

It can be observed that the difference in the concentration of the main alloying elements (Cr, Ni and Mo) in the austenite and ferrite phases was more significant in the welded joints with higher heat input (8 kJ/cm). This difference may be attributed to the low heat input welded joints remaining for a shorter time at high temperatures and being subjected to a higher cooling rate which causes a restriction in these elements' diffusivity.

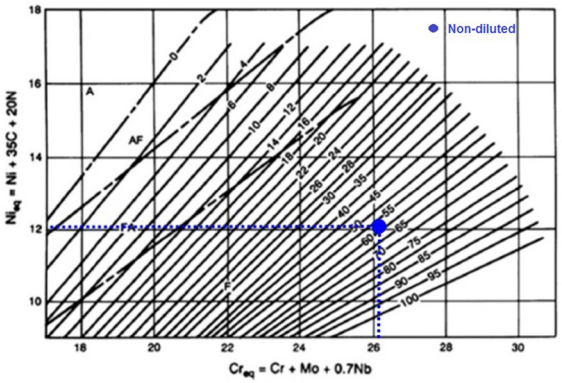

Figure 6. WRC-1992 diagram[28].

Table 3. Quantification of ferrite in the FZ with AWS ER2209 duplex stainless steel filler metal.

Heat input	4 kJ/cm		8 kJ/cm	
	Average value	Standard deviation	Average value	Standard deviation
Ferritoscope (%)	20.60	0.61	21.16	1.88

Table 4. Average values of the elements present in the austenitic and ferritic phases as a function of heat input.

Heat input	4 kJ/cm		8 kJ/cm	
Composition (%)	Austenite	Ferrite	Austenite	Ferrite
Si	0.40	0.41	0.46	0.49
Cr	22.84	23.24	21.98	24.60
Fe	63.39	63.28	63.00	62.41
Ni	10.24	9.62	11.37	8.19
Mo	3.14	3.45	3.19	4.32

3.2. Welded joints after AHT

Figures 7 and 8 show micrographs of the fusion zone of the welded joint using heat input of 8 kJ/cm and subjected to 50 and 100 hours of AHT, respectively.

Based on the analysis, it is possible to affirm that practically all ferrite present in the fusion zone before AHT was transformed into σ and χ phases. It is worthwhile pointing out that during the BSE-SEM analysis, the brightness and contrast were intentionally adjusted to potentialize the Z-contrast effect according to the capability of BSE emission of each phase due to the partitioning of refractory alloying element Mo. Therefore, it is possible to observe that the austenite grains (point 1) display a black colour due to its lower concentration in Mo. However, the precipitation of σ (point 2) and χ (point 3) phases together with austenite matrix were differentiated from each other due to their substantial difference in Mo.

Table 5 shows the chemical composition, obtained quantitatively by micro-analysis, through EDS, of the

reference points indicated in Figures 5 and 6. The results presented in each table again show the highest levels of Mo in the regions corresponding to points 2 and 3. As the χ phase particles have a significant amount of Mo, they display a white colour on the Figures, while the σ phase particles presented a light grey colour due to the intermediate concentration of Mo. Small regions displaying a dark grey colour were also observed together with the σ phase. These regions suggest being a portion of remaining ferrite which were not wholly transformed in σ and χ phases.

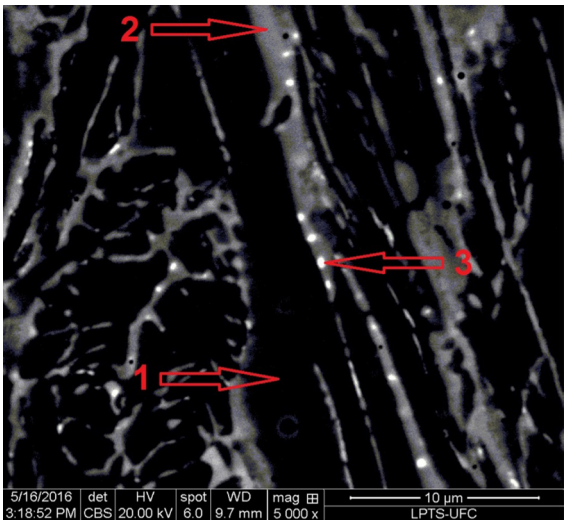

Figure 7. Microstructure of the zone fused with the AWS ER2209 electrode using energy of 8 kJ / cm with 50 hours of TTE. Highlight for phases (1) γ, (2) σ and (3) χ. No attack, MEV-BSE.

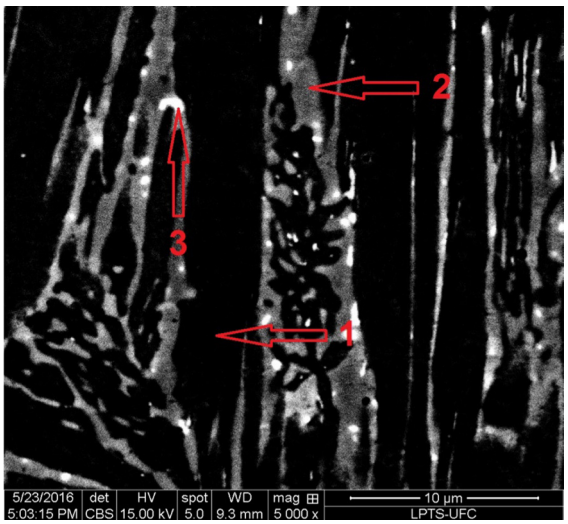

Figure 8. Microstructure of the zone fused with the AWS ER2209 electrode using energy of 8 kJ / cm with 100 hours of AHT. Highlighted phases (1) γ, (2) σ and (3) χ. No attack, MEV-BSE.

Table 5. Chemical composition by weight (%) of the austenite, sigma and chi phases in the FZ.

Phases	Si	Cr	Fe	Ni	Mo
1 - Austenite (γ)	0.40	21.76	63.04	11.39	3.41
2 - Sigma (σ)	0.56	33.36	57.00	3.51	5.57
3 - Chi (χ)	0.63	28.31	54.59	2.73	13.74

According to the literature[33,34], the σ and χ precipitation occur by diffusional phase transformation, being in some times governed by an eutectoid reaction of ferrite (α) → sigma (σ) + secondary austenite (γ_2). This phase transformation occurs preferably in ferrite due to some reasons. First, ferrite is specially enriched with elements such as Cr, Mo and Si, which are sigma formers. Second, the diffusivity of the sigma alloying elements Cr, Mo and si in ferrite is 100 times faster than in the austenite[35]. Third, the precipitation of the sigma phase through a cooperative eutectoid reaction becomes easier and faster.

According to Nilsson et al.[36], the precipitation temperature range of σ phase depends on the chemical composition of the alloy, but it is generally between 600 and 950 ºC. In duplex stainless steels, ferrite is thermodynamically metastable in the precipitation temperature range of phase σ. The preferred location for nucleation of the sigma phase in duplex stainless steels is the γ/α interfaces, due to the minor atomic breakdown that generates the orientation relationship adopted between the sigma phase and austenite, the sigma phase nucleates epitaxially in austenite and grows to ferrite[37].

For the two AHT times, it was possible to estimate that all ferrite has transformed in σ and χ phases. Thus, Table 6 presents the results obtained in the quantitative analysis of the precipitation of the σ and χ chi phases present in the fusion zone.

According to Table 6, the welded joints with higher heat input (8 kJ/cm) and aged for 50 hours presented the highest concentration of the χ phase (0.987%). However, when the aging time is raised up to 100 hours, the χ phase concentration presents the lowest content. According to the literature[38,39], for the longer aging time at 800 ºC, the χ phase content is reduced due to this phase is metastable and therefore consumed by the σ phase precipitation. Consequently, the content of σ phase is increased, as can be seen in the Table 6.

From the quantitative analysis showed in Table 6, it is also possible to infer that the welded joint using heat input of 8 kJ/cm and AHT time of 100 hours was the most critical condition due to its greater amount of deleterious phases. According to the literature[40], the precipitation of σ and χ phases is prone to reduce the toughness and elongation of duplex stainless steels.

In order to understand better the partition of the elements responsible for forming the phases in the fusion zone of the welded joint with 8 kJ/cm and aging time of 100 hours,

Table 6. Quantification of the austenite, sigma and chi phases in the fusion zone.

Heat input (kJ/cm)	Phases	AHT time (h)	
		50	100
4	**Austenite**	78.23±2.01	77.18 ± 1.96
	Sigma	20.85±2.12	22.47 ± 1.29
	Chi	0.925±0.69	0.344 ± 0.99
8	**Austenite**	79.12±1.63	74.67 ± 1.48
	Sigma	19.53±1.93	25.07 ± 1.79
	Chi	0.987±0.83	0.267 ± .081

Figure 9a presents a SEM-BSE micrograph, followed by the EDS micro-chemical mapping of this region. The EDS mapping highlights the concentration of the main elements present in the FZ. Changes in the elements Fe (Figure 9b), Cr (Figure 9c), Mo (Figure 9d), Ni (Figure 9e) and Si (Figure 9f) can be observed where the phases present significant changes in these elements, coinciding with the precipitated regions.

Again, the EDS mapping highlighted the peculiar partitioning behaviour between Mo and Ni at micro-scale. Mo is abundant inside the precipitates' region, which previously consisted of ferrite, while nickel presents small fractions in this same region. On the other hand, nickel was intensely concentrated within the austenite. Fe also showed slight chemical changes, with lower concentrations in the interdendritic regions and Si did not show any significant changes.

3.3. Tensile tests

Figures 10a-c and Table 7 show the results of the tensile tests performed on the dissimilar 317L welded joints. It is

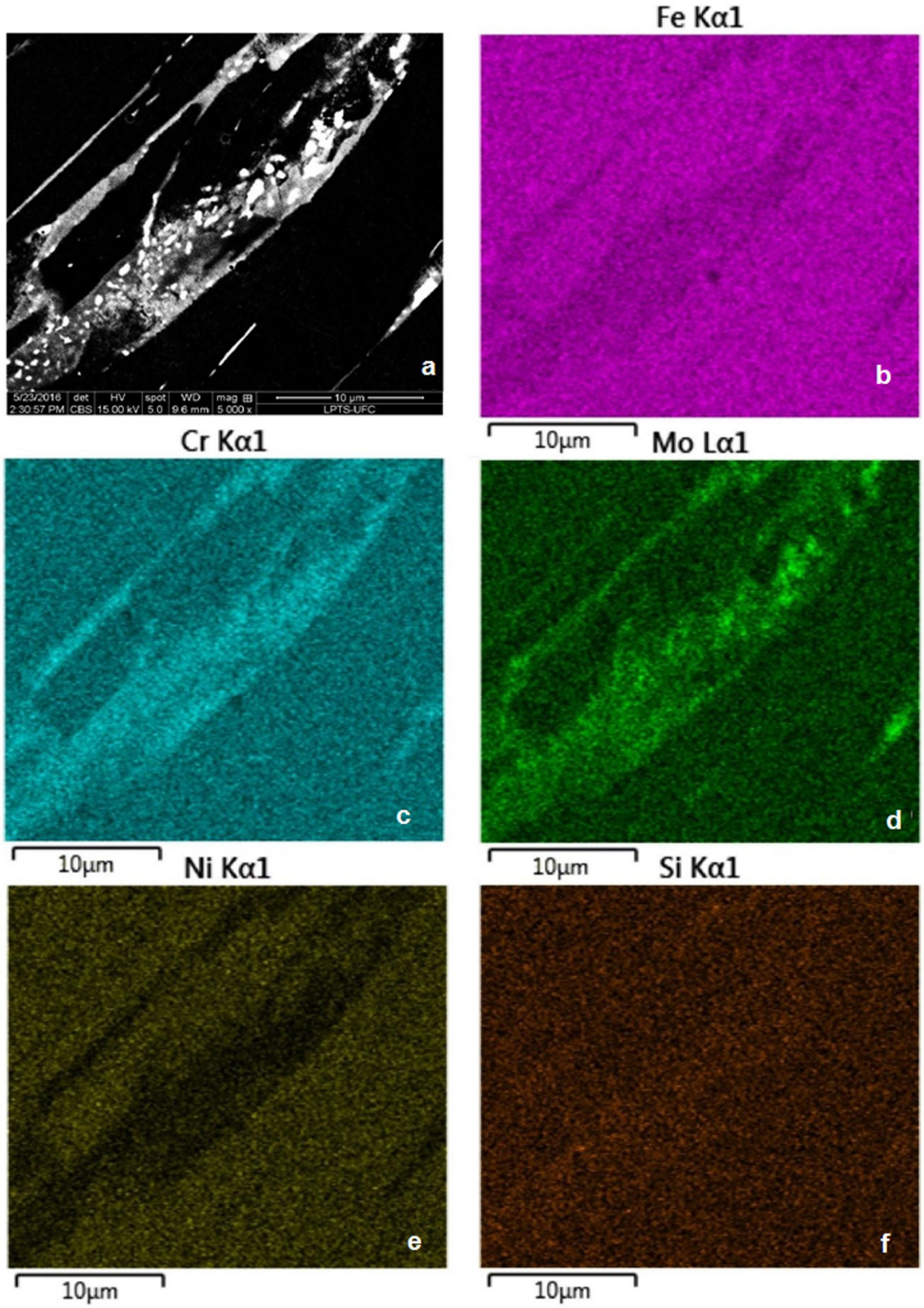

Figure 9. EDS mapping in the fusion zone using heat input of 8 kJ/cm and aged for100 hours.

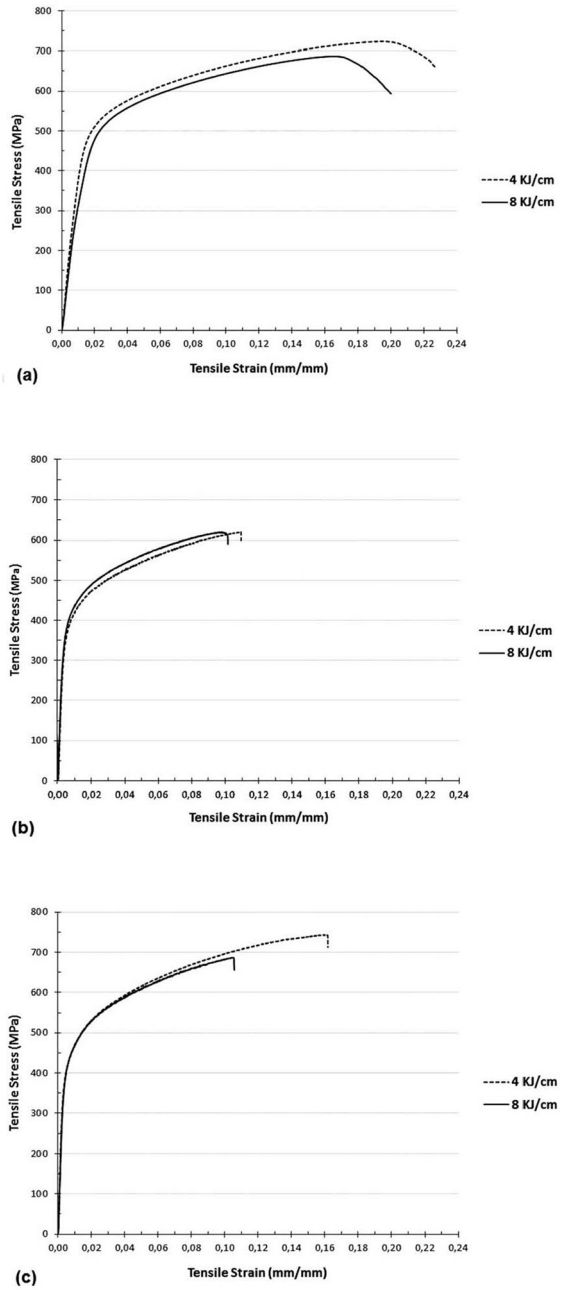

Figure 10. Stress-strain curve of tests performed on weldments with AWS ER2209 (a) without AHT, (b) with 50 h of AHT, and (c) with 100 h of AHT.

noted that the samples without AHT welded with lower heat input (4 kJ / cm) showed a slightly higher tensile strength, yield strength and ductility than the welded joints with higher heat input (8kJ/cm). Considering that the amount of ferrite in the FZ was practically the same for both heat inputs, a possible explanation for this slight difference in the mechanical behaviour is the more extensive HT-HAZ (134.3 ± 13.7 μm) and rougher microstructure verified in the welded joints using higher heat input (8 kJ/cm). In fact, all tensile samples failed in the HAZ and HAZ/FZ transition region in the ductile mode. It is known that during the thermal cycles arising from the welding process, the HAZ changes chemically, physically and metallurgically, which consequently deteriorates the microstructure and mechanical properties of the material[40].

Table 7 also shows that there was no significant influence of the heat input on the mechanical properties of the welded joints aged for 50 hours for both heat inputs. However, when the aging time is increased to 100 hours, the welded joints with lower heat input presented higher tensile strength and ductility. This behaviour may be mainly attributed to the lower concentration of δ-ferrite in the HAZ of the welded joints with 4 KJ/cm compared with the welded joint using 8 KJ/cm (see Figures 1 and 2). According to several works[38-41], higher percentage of the δ-ferrite in the HAZ significantly facilitates the hydrogen-induced embrittlement, being this hard phase the preferential path for cracks propagation.

Based on the results, it is also possible to notice that, in general, the AHT produced welded joints with higher mechanical properties than those before AHT. This is may be related to the increase in the precipitation of the σ phase with the increase of the AHT time. In several cases, the greater precipitation of this phase affects the welded joint's tensile strength and hardnesst due to the dispersion of hard σ phase particles into the ferrite and/or austenite grains[40,42,43]. However, it is worthwhile mentioning that the tensile properties results indicate that even though the precipitation of σ phase increases with the AHT time, its volume fraction is not enough to produce a significant loss of ductility.

3.4. Microhardness tests

Table 8 presents the results obtained in the microhardness tests along the cross-section of the dissimilar welded joints.

From the table, samples in the as-welded condition experienced a slight drop in the hardness values in the HAZ compared to the BM and FZ. This may be attributed to the absence of chromium carbides and nitrides (hard particles) in the HAZ. In fact, the high cooling rates experienced by

Table 7. Mechanical properties results.

AHT (hours)	Heat Input (kJ/cm)	Yield Limit (MPa)	Ultimate tensile strength (MPa)	Tensile Strain (%)
0 (unaged)	**4**	359.4 ± 12.0	728.4 ± 23.1	11.2 ± 4.2
	8	338.7 ± 16.2	694.0 ± 31.2	10.5 ± 3.1
50	**4**	358.1 ± 22.1	620.4 ± 0.7	12.1 ± 4.0
	8	368.1 ± 22.6	620.1 ± 17.5	12.7 ± 2.9
100	**4**	392.2 ± 30.4	743.0 ± 47.6	17.9 ± 1.7
	8	406.5 ± 3.2	687.2 ± 23.6	12.2 ± 2.8

Table 8. Microhardness profile of AISI 317L steel welded with the AWS ER2209 electrode using energies of 4 and 8 kJ / cm before and after AHT.

AHT (h)	Region	Heat input (kJ/cm)			
		4,0		8,0	
		Microhardness (HV_1)	Standard Deviation	Microhardness (HV_1)	Standard Deviation
0 (unaged)	**BM**	176.2	3.7	180.7	2.1
	HAZ	166.3	3.3	166.5	2.0
	FZ	220.8	15.1	212.6	8.8
50	**BM**	189.4	4.9	193.9	4.0
	HAZ	186.6	5.8	194.7	5.2
	FZ	305.8	9.9	274.8	12.3
100	**BM**	187.3	4.4	190.2	2.2
	HAZ	187.3	4.2	193.0	1.3
	FZ	339.0	9.0	340.5	7.1

the welded joints, as well as the low content of carbon and absence of nitrogen in the 317L base metal, did not favour the precipitation of these secondary phases. Another possible explanation is the higher amount of nickel (ductile element) in the austenite present in the HAZ once the 317L base metal presents nickel content considerably higher than the 2209 filler metal

In turn, the highest hardness values are verified in the FZ region. It is also possible to note that the hardness values in this region for both heat inputs are practically identical. This increase in hardness for the fusion zone can be correlated to the more significant amount of alloying elements and the higher ferrite content in this weld region.

Regarding the samples with AHT, the hardness results showed that there was no significant variation of the hardness in the base metal and HAZ of the aged welded joints for both times. Such behaviour is associated with the microstructural features of this zone, which is attributed to the high austenite contents, low fraction of ferrite and consequently low potential for solid-solution phase transformation from ferrite to sigma/chi phases.

The fusion zone (FZ), in turn, presented the highest hardness values and it was observed that this region acquired greater hardness with the increase in AHT time. This is directly related to the higher σ-phase content in this region. Again, it is worthwhile mentioning that in similar welding of 317L stainless steel, differently from this dissimilar welding, the hardness does not present significant variations in this region as a function of the heat input.

4. Conclusions

Based on the result about the welding and ageing of the AISI 317L/AWS ER 2209 dissimilar metal welds evaluated by microstructural characterization and mechanical properties, it can state the following conclusions:

The welded joints with higher energy (8 kJ/cm) and without AHT showed a more significant extension of the high temperature HAZ;

The thermal input did not influence the amount of ferrite precipitated in the FZ of the welded joints with the AWS ER2209 electrode;

The microstructure of the FZ of the welded joint with the AWS ER2209 electrode (without AHT) showed a large amount of austenite that precipitated in three different primary morphologies: allotriomorphic of grain boundary, Widmanstätten and intragranular;

For all heat-treated samples, it was possible to identify the presence of phases σ and χ, so that the highest concentration of phase χ was identified in samples submitted to 50 hours of AHT;

In the tensile tests, all welded joints showed an increase in the tensile strength and yield limit after the thermal ageing treatment;

The welding condition and thermal treatment of ageing that presented joints with superior mechanical resistance and toughness were the samples welded with heat input of 4 kJ / cm and heat-treated for 100 hours;

In microhardness tests, all welded joints showed an increase in the hardness profile after the ageing heat treatment;

The microhardness values found showed a good correlation with the microstructure and the tensile tests, sothe highest hardness values were observed in the fusion zone of the welded joints with AHT.

5. Acknowledgments

The authors are grateful to the Materials Laboratory of the Federal University of Itajubá, and the Welding Research and Technology Laboratory of the Federal University of Ceará for the facilities and the Federal Center for Technological Education of Minas Gerais (CEFET-MG), CNPq, CAPES and FAPEMIG for the financial support.

6. References

1. Tuttle RN. Corrosion in oil and gas production. J Pet Technol. 1987;39(7):756-62.
2. Popoola LT, Grema AS, Latinwo GK, Gutti B, Balogun AS. Corrosion problems during oil and gas production and its mitigation. Int J Ind Chem. 2013;4(35):35.
3. Silva CC, Farias JP, de Sant'Ana HB. Evaluation of AISI 316L stainless steel welded plates in heavy petroleum environment. Mater Des. 2009;30(5):1581-7.
4. Medvedeva ML. Specifics of high-temperature corrosion processes during oil recovery. Chem Petrol Eng. 2000;36(11-12):749-54.

5. Slavcheva E, Shone B, Turnbull A. Review of naphthenic acid corrosion in oil refining. Br Corros J. 1999;34(2):125-31.
6. Silva CC, Machado JPSE, Sobral-Santiago AVC, Sant'Ana HB, Farias JP. High-temperature hydrogen sulfide corrosion on the heat-affected zone of the AISI 444 stainless steel caused by Venezuelan heavy petroleum. J Petrol Sci Eng. 2007;59(3-4):219-25.
7. Lo KH, Shek CH, Lai JKL. Recent developments in stainless steels. Mater Sci Eng Rep. 2009;65(4-6):39-104.
8. Silva CC, Miranda HC, Sant'Ana HB, Farias JP. Austenitic and ferritic stainless steel dissimilar weld metal evaluation for the applications as-coating in the petroleum processing equipment. Mater Des. 2013;47:1-8.
9. Farneze HN, Tavares SSM, Pardal JM, Barbosa C, Pereira OC, Cunha RPC. Effects of aging at 450ºC on the pitting corrosion resistance and toughness of AISI 317L steel welded by GTAW and FSW. Mater Res. 2017;20(Suppl. 2):621-9.
10. Silva CC, Miranda HC, Sant'Ana HB, Farias JP. Microstructure, hardness and petroleum corrosion evaluation of 316L/AWS E309MoL-16 weld metal. Mater Charact. 2009;60(4):346-52.
11. Verma J, Taiwade RV. Effect of austenitic and austeno-ferritic electrodes on 2205 duplex and 316L austenitic stainless steel dissimilar welds. J Mater Eng Perform. 2016;25(11):4706-17.
12. Touileb K, Hedhibi AC, Djoudjou R, Ouis A, Bensalama A, Ibrahim A, et al. Mechanical, microstructure, and corrosion characterization of dissimilar austenitic 316l and duplex 2205 stainless-steel ATIG welded joints. Materials. 2022;15(7):2470.
13. Neissi R, Shamanian M, Hajihashemi M. The effect of constant and pulsed current gas tungsten arc welding on joint properties of 2205 duplex stainless steel to 316L austenitic stainless steel. J Mater Eng Perform. 2016;25(5):2017-28.
14. Albuquerque VHC, Cortez PC, Alexandria AR, Aguiar WM, Silva EM. Sistema de segmentação de imagens para quantificação de microestruturas em metais utilizando redes neurais artificiais. Materia. 2007;12(2):394-407.
15. Mina ME, Cruz SY, Ferreira MM, Miranda HC, Dille J, Silva CC. Electron detection modes comparison for quantification of secondary phases of inconel 686 weld metal. Mater Charact. 2017;133:10-6.
16. Nunes EB, Alves FN Jr, Miranda HC, Farias JP, Habreu HFG, Silva CC, et al. Efeito da energia de soldagem sobre a microestrutura e propriedades mecânicas da zona afetada pelo calor de juntas de aço inoxidável duplex. Soldag. Insp, Sao Paulo. 2011;16(3):223-31.
17. Antunes PD, Correa EO, Barbosa RP, Silva EM, Padilha AF, Guimaraes PM. Effect of the weld metal chemistry on stress corrosion cracking behaviur of AISI 444 ferritic stainless steel weldments in boiling chloride solution. Materials Corrosion. 2013;64(5):415-21.
18. Aguilar S, Tabares R, Serna C. Microstructural transformations of dissimilar austenite-ferrite stainless steels welded joints. J Materials Physics and Chemistry. 2013;1(4):65-8.
19. Antunes PD, Silva CC, Correa EO, Tavares SMM. Influence of the heat input and aging treatment on microstructure and mechanical properties of AISI 317 L steel weldments using 0020 robotic–pulsed GMAW. Int J Adv Manuf Technol. 2019;105(12):5151-63.
20. Brooks JA, Yang NCY, Krafcik JS. Clarification on development of skeletal and lathy ferrite morphologies in stainless steel welds. Sci Technol Weld Join. 2001;6(6):412-4.
21. Silva RS, Demarque R, Santos EP, Castro JA. Influence of heat input on the characteristics and properties of AISI 316 and AISI 316L steels weld beads. Soldag Insp. 2020;25:1-13. https://doi.org/10.1590/0104-9224/SI25.04.
22. Tavares SSM, Feijó GF, Farneze HN, Sandim MJR, Souza IR Fo. Influence of microstructure on the corrosion resistance of AISI 317L (UNS S31703. Mater Res. 2017;20(Suppl. 2):108-14.
23. Schaeffler AL. Constitution diagram for stainless steel weld metal. Metal Prog. 1949;56(11):680.
24. Lippold JC, Kotecki DJ. Welding metallurgy and weldability of stainless steels. New Jersey: John Wiley & Sons; 2005.
25. Yurtisik K, Tirkes S, Dykhno I, Gur CH, Gurbuz R. Characterization of duplex stainless steel weld metals obtained by hybrid plasma-gas metal arc welding. Soldag Insp. 2013;18(3):207-16.
26. Zappa S, Zalazar M, Surian E. Efecto de la composición química del metal de aporte y del calor aportado sobre la microestructura y las propiedades mecánicas de juntas soldadas de aceros inoxidables dúplex. Soldag Insp. 2017;22(2):116-28.
27. Rodrigues CEAL, Azevedo AGL, Silva CC, Farias JP. Mechanical and metallurgical evaluation of ANSI/AWS A5.4-06 E309 weld metals. Soldag Insp. 2008;13(1):32-45.
28. Kotecki DJ, Siewert TA. WRC-1992 Constitution Diagram for Stainless Steel Weld Metals: A Modification of the WRC-1988 Diagram. Weld J. 1992;71(5):171s-8s.
29. Muthupandia V, Srinivasan PB, Shankar V, Seshadri SK, Sundaresan S. Effect of nickel and nitrogen addition on the microstructure and mechanical properties of power beam processed duplex stainless steel (UNS 31803) weld metals. Mater Lett. 2005;59(18):2305-9.
30. Lindblom BES, Lundqvist B, Hannerz NE. Grain growth in HAZ of duplex stainless steels. Scand J Metall. 1991;20:305-15.
31. Menezes AJW, Abreu H, Kundu S, Bhadeshia HKDH, Kelly PM. Crystallography of Widmanstätten austenite in duplex stainless steel weld metal. Sci Technol Weld Join. 2009;14(1):4-10.
32. Atamert S, King JE. Intragranular nucleation of austenite. Z Metallk. 1991;82(3):230-9.
33. Plaut RL, Herrera C, Escriba DM, Rios PR, Padilha AF. A short review on wrought austenitic stainless steels at high temperatures: processing, microstructure, properties and performance. Mater Res. 2007;10(4):453-60.
34. Villanueva DME, Pimenta FC Jr, Plaut RL, Padilha AF. Comparative study on sigma phase precipitation of three types of stainless steels: austenitic, superferritic and duplex. Mater Sci Technol. 2006;22(9):1098-104.
35. Padilha AF, Rios PR. Decomposition of austenite in austenitic stainless steels. ISIJ Int. 2002;42(4):325-27.
36. Nilsson JO, Jonsson P, Wilson A. Formation of secondary austenite in superduplex stainless steel weld metal and its dependence on chemical composition. In: 4th International Conference Duplex Stainless Steels; 1994; Glasgow, Scotland. Proceedings. Cambridge: Abington Pub.; 1994.
37. Srutt AJ, Lorimer GW. Structure property relationships of zeron 100. In: International Conference on on Duplex Stainless Steels'86; 1986; The Hauge, The Netherlands. Proceedings. Zutphen: KCI Publishing; 1986. p. 310-8.
38. Escriba DM, Materna-Morris E, Plaut RL, Padilha AF. Chi phase precipitation in a duplex stainless steel. Mater Charact. 2009;60(11):1214-9.
39. Pohl M, Storz O, Glogowski T. Effect of intermetallic precipitations on the properties of duplex stainless steel. Mater Charact. 2007;58(1):65-71.
40. Miloud MH, Bahri OC, Ali B, Mohamed B, Benattou B. Effect of the mechanical properties and mode loading on the mechanical behaviour of weldment: a numerical analysis. Mater Res. 2013;16(4):853-9.
41. AmaroVicente T, Oliveira L, Correa E, Barbosa R, Macanhan V, Alcântara N. Stress corrosión cracking behaviour of dissimilar welding of AISI 310S austenitic stainless steel to 2304 duplex stainless steel. Metals. 2018;8(3):195.
42. Kazasidis ME, Pantelis DI. The effect of the heat input energy on the tensile properties of the AH-40 fatigue Crack arrester steel, welded by use of the robotic metal –cored arc welding technique. Int J Adv Manuf Technol. 2017;93(9-12):3967-80.
43. Farneze HN, Tavares SSM, Pardal JM, Nascimento RF, Abreu HFG. Degradation of mechanical and corrosion resistance properties of AISI 317L steel exposed at 550 °C. Eng Fail Anal. 2016;61:69-76.